Volume 1 | Number 1 | Jan 2013 | Pages 1–100

Nanoscale

www.rsc.org/nanoscale

ROYAL SOCIETY OF CHEMISTRY

ROYAL SOCIETY OF CHEMISTRY

www.rsc.org/nanoscale

Tailoring water structure and transport in nanotubes

with tunable interiors

Luis Ruiz[†], Yuanqiao Wu[‡], and Sinan Keten*

[†]Dept. of Mechanical Engineering, Northwestern University, 2145 Sheridan Road, Evanston, IL

60208-3109

[‡]Dept. of Civil and Environmental Engineering, Northwestern University, 2145 Sheridan Road,

Evanston, IL 60208-3109

* Corresponding Author: Dept. of Civil & Environmental Engineering and Dept. of Mechanical

Engineering, Northwestern University, 2145 Sheridan Road, Evanston, IL 60208-3109. Tel: 847-

491-5282, Email: *s-keten@northwestern.edu*

Table of Contents
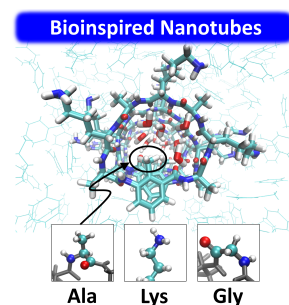
The organization and transport properties of water in nanotubes can be tailored by bioinspired

chemical functionalization of the nanotube lumen.

Abstract

Self-assembly of cyclic peptide nanotubes (CPNs) in polymer thin films has opened up the possibility to create separation membranes with tunable nanopores that can differentiate molecules at the sub-nanometer level. While it has been demonstrated that the interior chemistry of the CPNs can be tailored by inserting functional groups in the nanopore lumen (mCPNs), a design strategy for picking the chemical modifications that lead to particular transport properties has not been established. Drawing from the knowledgebase of functional groups in natural amino acids, here we use molecular dynamics simulations to elucidate how bioinspired mutations influence the transport of water through mCPNs. We show that, at the nanoscale, factors beside the pore size, such as electrostatics interactions and steric effects, can dramatically change the transport properties. We recognize a novel asymmetric structure of water under nanoconfinement inside the chemically functionalized nanotubes and identify that small non-polar Glycine-mimic groups that minimize the steric constraints and confer a hydrophobic character to the nanotube interior are the fastest transporters of water. Our computational thought experiments on a realistic material concept circumvents synthetic challenges, and lay the foundation for bioinspired principles to tailor artificial nanochannels for separation applications such as desalination, ion-exchange and carbon capture.

Keywords: molecular dynamics, nanotube, water transport, bioinspiration, cyclic peptide

Introduction

Today, there is a growing need for environmentally friendly separation membranes to address some of society's most pressing issues associated to molecular selective transport applications such as carbon capture, water desalination or fuel cell technology [1-4]. In pursuit of overcoming some of the limitations of conventional nanoporous membranes, namely, control of the pore size distribution and

pore continuity across the membrane, composite systems with carbon nanotubes (CNTs) embedded in an impermeable polymer matrix have been proposed [5-8]. However, despite the promise of CNTs as fast transporters, tailoring their interior surface chemistry still remains challenging. This lack of tunability restricts the implementation of biomimetic concepts that could otherwise improve the selectivity and functionality of the membranes. Biological channels are a great source of inspiration as they display great control over the molecular selectivity that arises from their chemical heterogeneity. Prime examples include Aquaporins, ion channels or bacterial porins such as Gramicidin [9-11]. However, in order to be able to implement biomimetic concepts to engineered systems, a synthetic platform that allows more design flexibility is required.

Organic nanotubes formed by stacked cyclic peptides stabilized by hydrogen bonds (cyclic peptide nanotubes, or CPNs), are particularly promising candidates as biomimetic synthetic nanopores due to their exceptional mechanical properties, possible control over the pore size at the sub-nanometer level, and highly tunable chemistry [12-15]. Flexible thin nanoporous membranes containing vertically aligned subnanometer CPNs have been generated by co-assembling polymer conjugated cyclic peptides in block copolymer micro domains [7], validating the feasibility of the design. Furthermore, the possibility of chemical functionalization of the CPN lumen by insertion of an unnatural amino acid in the peptide sequence containing a functional group that points towards the interior of the ring (referred as modified cyclic peptides, or mCPs) has been recently unveiled [14]. This synthetic route opens the door to the application of biomimetic concepts to engineered nanotubes, and that, together with the commensurability of the inter-ring spacing with the distances between functional groups observed in biological systems, render mCPNs as a unique platform to test biomimetic designs and investigate features of biological channels.

The study of water permeation through biological and synthetic nanochannels has been a prevalent topic of discussion in recent years due to the importance of water purification applications and the biological relevance of the problem [16-24]. Under nanoscale confinement, water has been observed to display physical attributes substantially different than those of the bulk, leading to transport properties that differ greatly from the predictions of classical continuum theories [25-28]. For example, it has shown that the flux of water under one dimensional nanoconfinement in carbon nanotubes greatly exceeds classical hydrodynamic predictions [25], highlighting the potential of sub-nanometer hydrophobic channels as high throughput systems for molecular transport applications. Another important aspect to consider besides the size of the channel is the interior chemistry. It has been shown in idealized nanochannels that water permeability is maximized for intermediate values of the interaction between the pore and the water. While highly polar interiors (i.e. hydrophilic pore) facilitate the entry of water, the translocation across the channel is diminished due to the fact that water molecules spend longer times inside the pore. On the other hand, low polar interiors (i.e. hydrophobic pore) impose a solvation energy barrier that reduces the entrance of molecules into the pore, resulting again in low permeability.

The structure and transport properties of water through conventional CPNs have been previously studied [29-32]. However, due to the novelty of the synthetic route to chemically functionalize the cyclic peptides, the molecular transport properties of the most promising mCPNs remain currently unexplored. Here, we employ computational modeling to test bioinspired designs in an engineering platform beyond the physiological context. We aim to understand the role that the chemistry of the functional group in the mutated amino acid plays on the organization and permeability of water in bioinspired mCPNs. To elucidate this, we use atomistic Molecular Dynamics (MD) simulations under equilibrium conditions and different levels of hydrostatic pressure (Fig. 1a). We sample a variety of functional groups to gain a complete understanding, specifically, we use chemistries

mimicking deprotonated Lysine (large, polar), Glycine (small, non-polar), and Alanine (large, non-polar) amino acid side-chains (Figure 1b). The charge distributions of the different functional groups are shown in Figure S1. In the following sections of the paper we present, first, a summary of the computational methodology employed. Next, we analyze the structure of water inside the nanotubes and reconstruct the energy profiles of water along the pores. Finally, we identify the best performers in terms of unidirectional water permeation under pressure, and link the performance to the specific structural features of the mCPNs. The results provided here would help guide experimental efforts towards suitable nanotube designs.

(a)

(b)
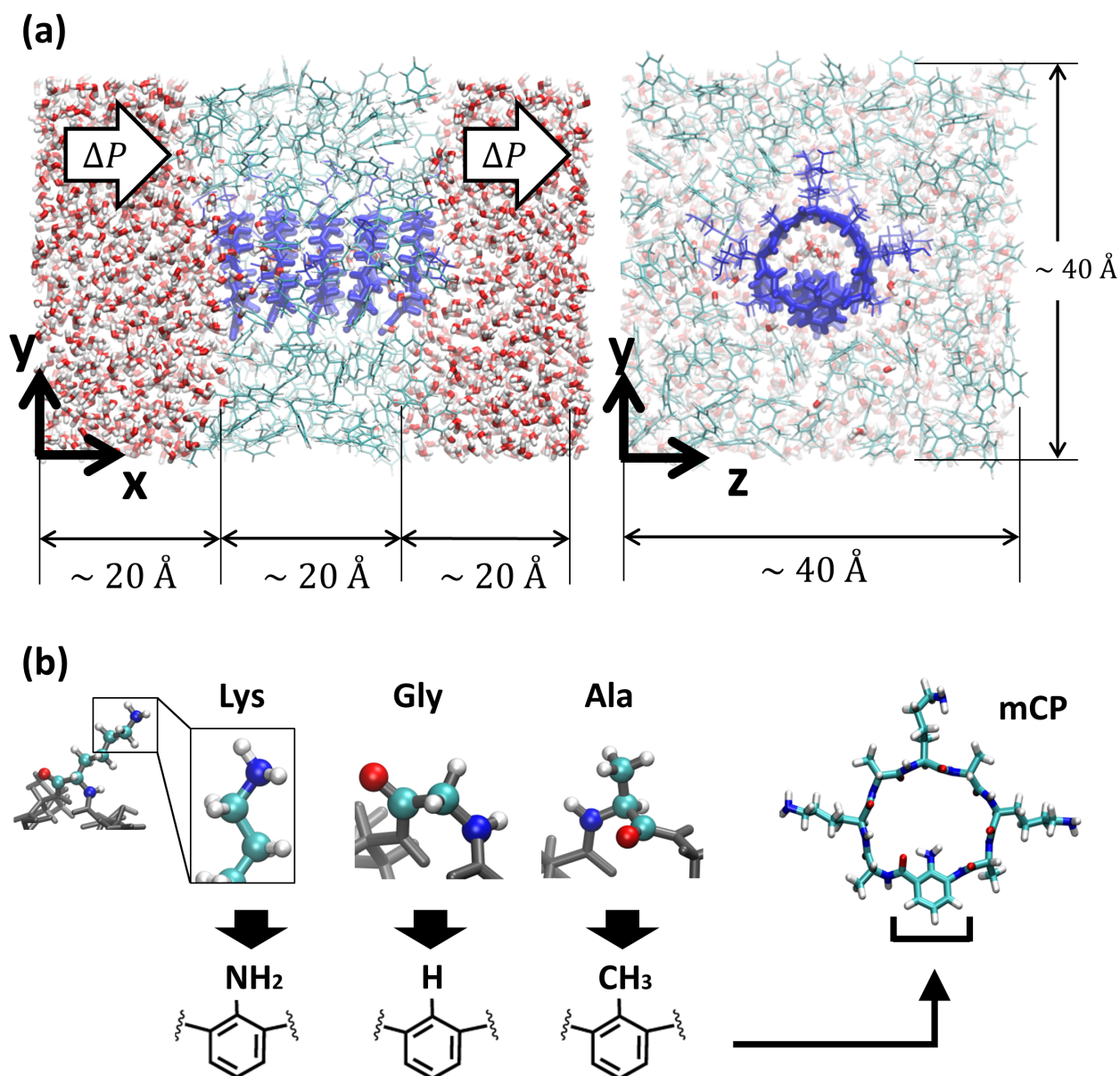
Figure 1. Molecular model of the system. (a) Different views of the nanotube (dark blue) embedded in a low dielectric membrane made of toluene restrained in a glass state to be impermeable (light blue), and solvated in water (oxygen atoms in red and hydrogen atoms in white). For clarity, the water in front of the membrane in the yz-plane view has been removed. Periodic boundary conditions are applied in all directions. (b) Schematics of the different bioinspired functional groups attached to the unnatural amino acid, and a snapshot of a mCP-Lys.

Results and discussion

First, we analyze the distribution and orientation of the water molecules inside the different mCPNs. The organization of water has a critical impact in the transport and selectivity properties of nanotubes since it governs aspects such as the coordination of ions inside the pores or the transport mechanism of water molecules (e.g. the single-file water structure requires concerted motion inside the pore for translocation) [29, 33, 34]. The orientational configuration of water also has implications on the transport properties of the nanotubes. For example, the dipole inversion of the single-file water wire can prevent proton transport through Grotthuss mechanism, as is the case for Aquaporins [35].

The density profiles of water along the different nanotubes (Fig. 2a), as well as the cross-sectional density heat maps (Fig. 2b), show that the water molecules preferentially occupy the interring spacing, opposed to the C_α-plane regions. This structure occurs for both the conventional CPN and the different mCPNs, and it is a result of the combination of steric constraints imposed by the cyclic peptide backbone and favorable interactions between the water molecules and the carbonyl groups of the peptides. To illustrate how the size and chemistry of the functional group shapes the configuration of water in the cross-section of the nanotubes, we build density heat maps that show the probability of occurrence of water molecules on the ring plane and the inter-ring regions (Fig. 2b). Along the y-axis, an asymmetric distribution is observed. The water molecules, pushed by functional group, tend to occupy the upper part of the nanotube, particularly in the C_α ring plane regions (Fig 2d). The asymmetry of the distribution is more pronounced for the large, hydrophobic functional group (mCPN-Ala), suggesting that steric constraints are the cause of the shift of the distribution (Fig. S2). The chemistry of the functional group also plays a role determining the wettability of the pore. Favorable interactions between the water molecules and the NH_2 group in the mCPN-Lys, drive water molecules to occupy the space closer to the functional group. Along the z-

axis, the heat maps show highly populated regions on both sides of the functional group. A closer look to the probability distributions reveals that water molecules tend to concentrate on the side of the carbonyl group of the unnatural amino acid (Fig. S3). Due to the antiparallel stacking of the rings, the location of the carbonyl group alternates along the nanotube, affecting the distribution of water molecules. Our analysis suggests that the polarity and the steric repulsions imposed by the functional group, together with electrostatic interactions between the carbonyl groups and the water molecules, are responsible for the arrangement of water molecules in this fashion inside the nanotubes. The asymmetric water structure that we just described has not been previously observed and it is substantially different than that in conventional CPNs or carbon nanotubes (CNTs) of equivalent size (e.g. (8,8) with a diameter of ~1 nm), characterized by cylindrically symmetrical density distributions [30, 36].

(a)

(b)
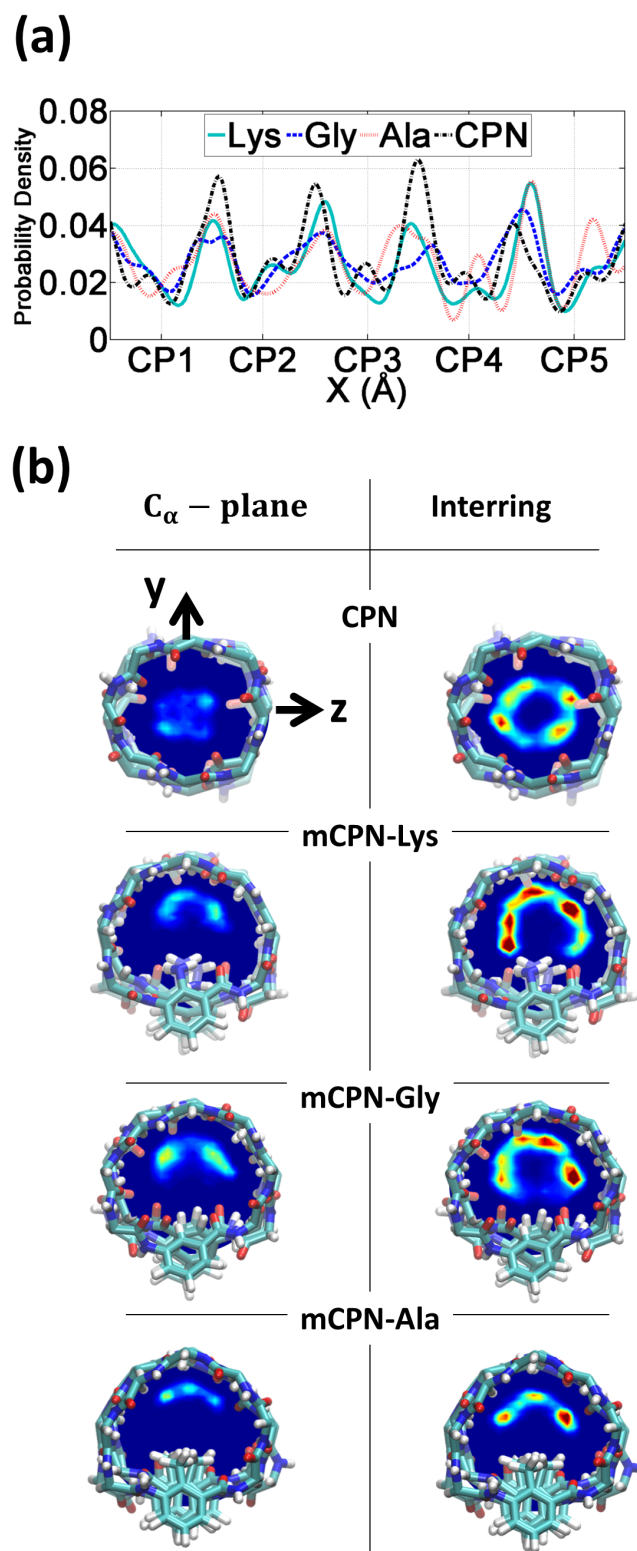
Figure 2. Distribution of water inside the nanotubes. (a) Probability density profile along the nanotube axis. (b) Mean density heat maps of water averaged over the regions corresponding to the

C_α-plane of the rings (left) and the inter-ring regions (right). In the color scale red indicates higher occupancy of water while dark blue indicates no water molecules.

Next, we analyze the orientation of water molecules inside the nanotube and the electrostatic signature of the different systems. The orientation angle of the water molecules with respect to the axis of the nanotube is characterized by the existence of very distinctive peaks in the probability distribution at approximately 30° and 150° on the left and right ends of the nanotube respectively (regions R1 and R3 as shown in Figure 3). The strong orientation at the ends of the nanotube arises from the tendency of the water dipoles to align with the electrostatic potential, higher in the membrane and zero in the water reservoirs (Fig. 4a). The symmetrical angle on both ends of the nanotube implies a dipole inversion upon translocation, corroborating previous studies on CPNs [30, 32]. Due to the symmetry of the system, the center of the nanotube (region R2 in Figure 3) is where the dipole inversion is expected to occur, leading to a flat probability distribution of the orientational angle in this region. This is the case for the CPN, mCPN-Lys, and the mCPN-Gly. On the other hand, the orientation angle distribution in the central region of the mCPN-Ala shows a bimodal shape (Fig. 3). This can be explained by the distinct electrostatic signature of this system that exhibits a minimum in the center of the nanotube, a feature that is not displayed by the other types of mCPNs (Fig. 4b). This minimum in the electric potential generates gradients of opposite directions that may cause the bimodal shape of the orientation angle distribution. A snapshot of the water molecules inside the mCPN-Ala illustrates the situation (Fig. 5d).
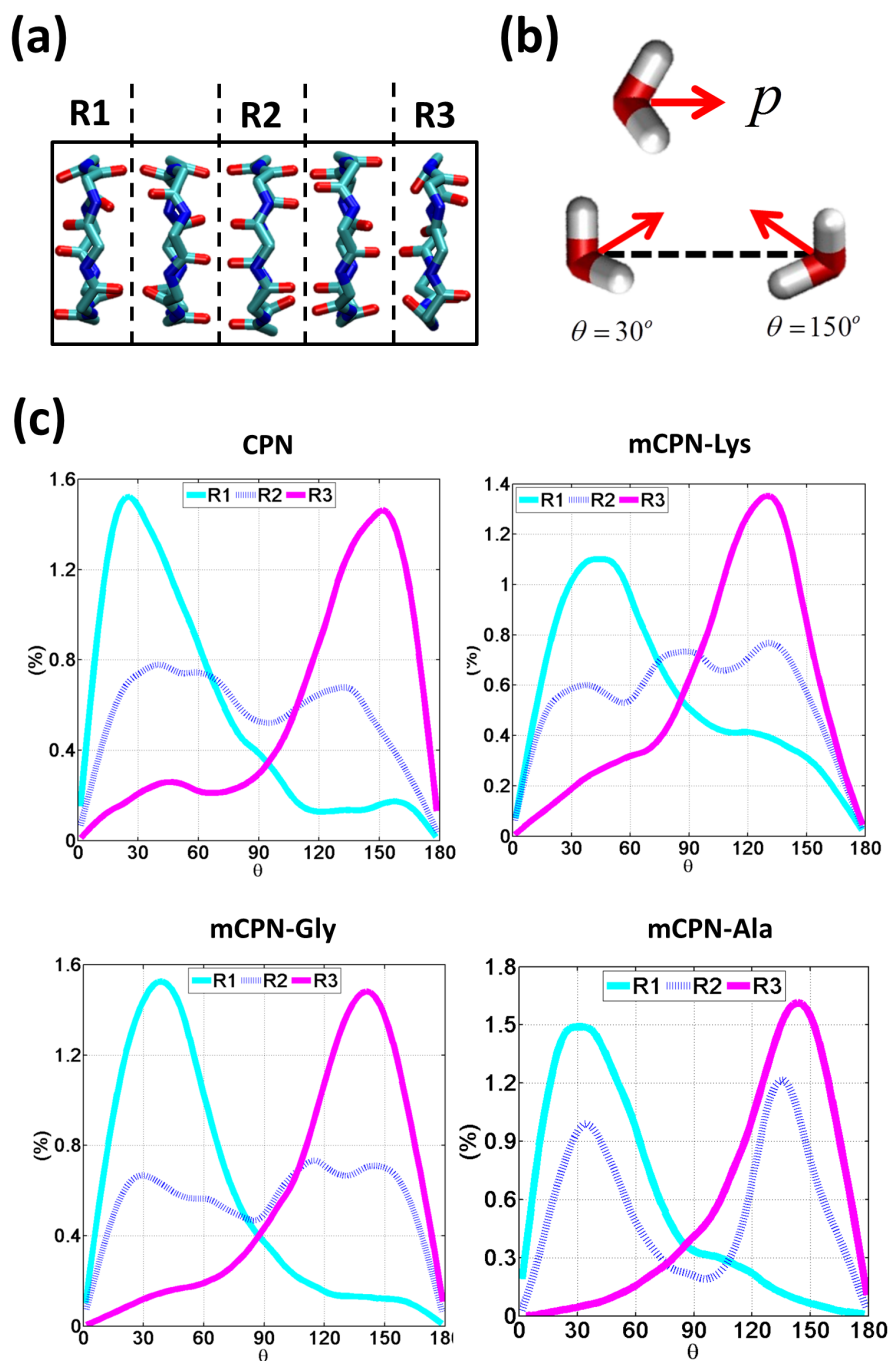
Figure 3. Water orientation inside the nanotubes. (a) Schematic of the 3 regions in which the nanotube has been divided to measure the regional dipole orientation. (b) Schematic representation of the dipole moment of a water molecule and illustrative snapshots of a water molecule oriented at 30° and 150°. (d) Probability distributions of water dipole orientation angle with respect to the nanotube axis for the different regions.

(a)

(b)
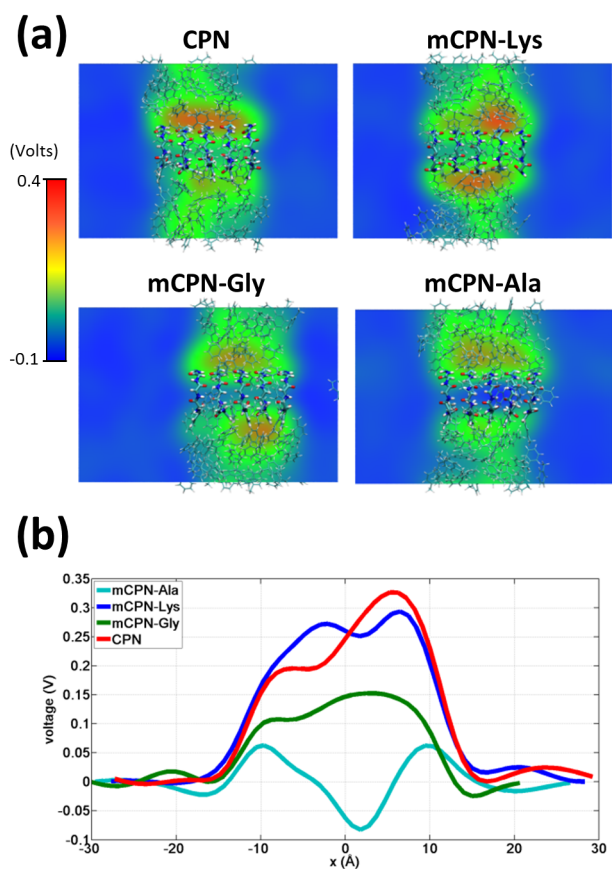
Figure 4. Electrostatic signature of the different systems. (a) Heat maps of the average local electrostatic potential on a cut through the nanotube centers. (b) One-dimensional voltage profiles along the nanotubes.
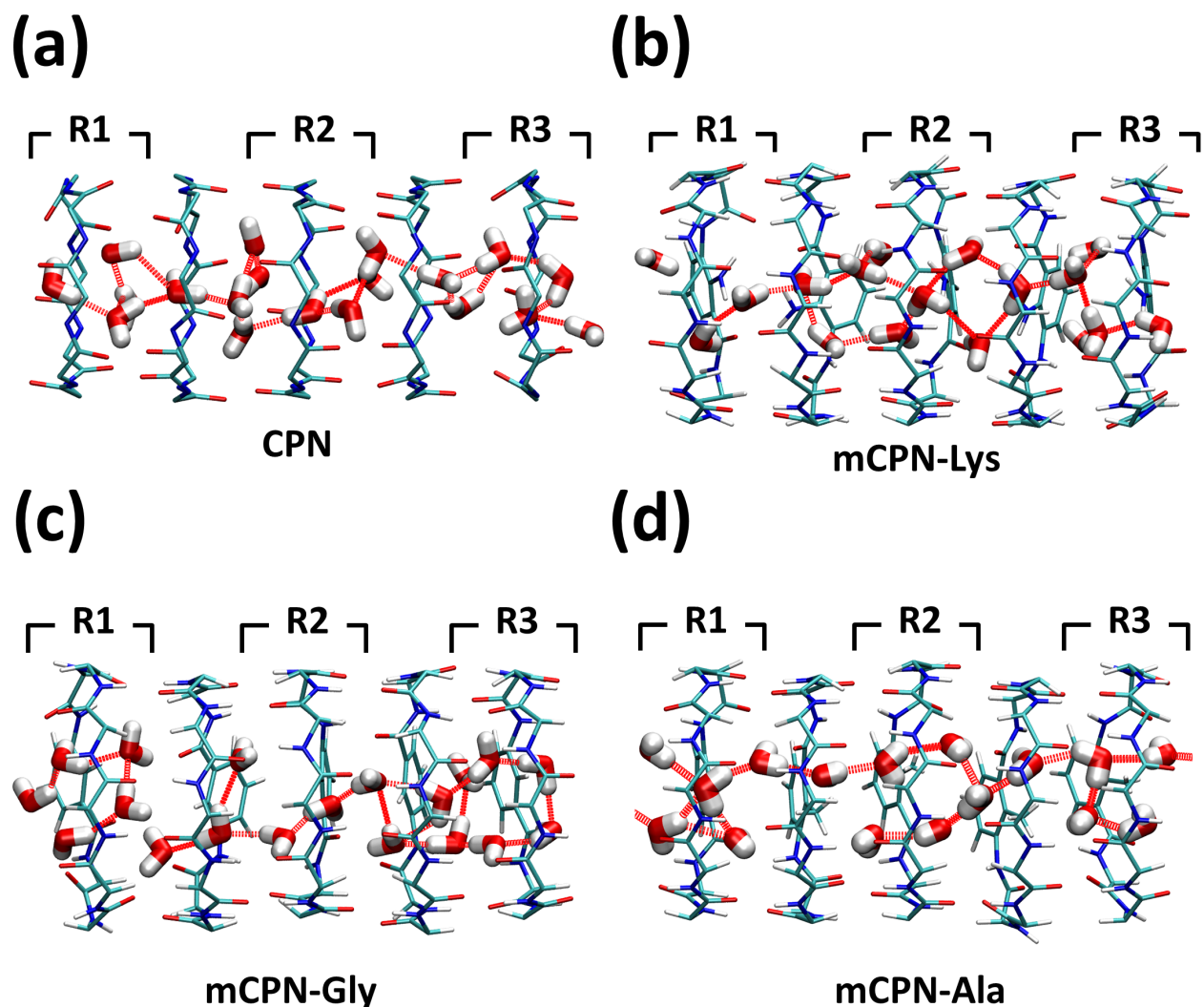
Figure 5. Snapshots of water structure inside the (a) CPN, (b) mCPN-Lys, (c) mCPN-Gly, and (d) mCPN-Ala. Hydrogen bonds between the water molecules are shown as dashed red lines.

A question that persists in the literature of molecular transport under nanoconfinement is whether classical continuum theories can be applied to predict flow rates in nanochannels. For example, can two pores with similar pore diameters exhibit distinctly different flow rates? The diameter of the pore controls occupancy, that is, the number of molecules that can be accommodated on average within the nanochannel. Here, we examine the occupancy and the permeability of the different nanotubes under applied pressure and compare it to simple hydrodynamic predictions of the Hagen-Poiseuille equation.

We observe that the occupancies of the mCPNs are mainly controlled by the size and polarity of the functional groups, with small size and higher polarity leading to higher occupancy. The mCPN-Ala, which contains large hydrophobic groups, displays an occupancy of ~12 molecules, the lowest of all the cases studied (Fig 6b). On the other hand, the mCPN-Gly, containing small hydrophobic groups, exhibits similar occupancy that the case with large hydrophilic groups, mCPN-Lys (~17 molecules), suggesting that steric effects can be compensated with the hydrophilicity of the functional group. These nanotubes display similar occupancies despite the fact that their interior volume is different (large functional groups lead to smaller interior volume and vice versa). This observation is in clear contrast to the macroscopic viewpoint where channels with similar occupancies necessarily imply similar interior volumes, and highlights the critical role that the chemistry plays at the nanoscale.

In order to quantify the permeability through the different nanotubes, we define net flux and flow of water. We define net flux as the difference between the number of permeation events in the (+x) (direction of the gradient of the applied pressure) and (–x) directions: $flux = (+x) - (-x)$. Flow, on the other hand, is defined as the sum of the permeation events in both directions: $flow = (+x) + (-x)$. Figure 6a shows the water flux as a function of the applied pressure for the different nanotube chemistries. The data can be fit by a linear trend with reasonably accuracy, suggesting that while the nanoscale flow is not expected to strictly follow the Hagen-Poiseuille (HP) equation (the continuum hydrodynamics equation governing laminar flow along a circular pipe), the mass transport relationship $Q \sim \Delta P$, where Q is volumetric flux and ΔP pressure difference, still holds for the wide range of pressure differences studied here. This scaling relationship has also been shown to hold at the nanoscale in previous computational studies on CPNs [31] and CNTs [37]. The flux in mCPNs (Fig. 6a) is comparable to that of biological systems over comparable lengths, with Aquaporins displaying a flux of ~1-2 water molecules per nanosecond under physiological osmotic

pressure (approximately equivalent to a hydrostatic pressure of 10 MPa) [38], and Aquaglyceroporins

exhibiting a flux of ~5ns[-1] for a pressure of P=197 MPa according to a computational study [39]. It is

worth mentioning that, while ballpark comparisons between different studies and methodologies

may be acceptable if done with care, precise quantitative comparisons should be avoided due to the

possible dependence of the results from the different studies on simulation parameters and system

set-up.

We also put to the test the scaling $Q \sim R^4$ of the HP equation. The interior volume of the nanotubes

can be determined using $V_{int} = O_{H_2O} \cdot v_{H_2O}$, where O_{H_2O} is the occupancy number, and v_{H_2O} is the

volume of a water molecule. The volume of the channel scales with the radius as $V_{int} \sim R^2$.

Therefore the scaling of the HP equation between the flux and the occupancy number is $Q \sim \left(O_{H_2O}\right)^2$

. The normalized flux versus occupancy data, together with the prediction of the HP equation is

shown in Figure 6c. We find certain correlation between the occupancies of the different nanotubes

and their flux, with lower occupancy leading to lower permeability and vice versa. The exact

relationship is unclear, and the HP equation seems unable to capture the trend. This highlights the

fact that at the nanoscale, other aspects besides the dimensions of the pore (e.g. the volume), such as

steric constraints and electrostatic effects that shape the energy profile of water flowing through the

nanotube, play important roles determining the permeability through the nanotubes. For example,

mCPN-Gly and mCPN-Lys exhibit very similar occupancy values, although the permeability is very

different between both.

Another important aspect of nanoscale molecular transport is the efficiency of the systems on

transporting water in a unidirectional fashion. It has been observed in CNTs that thermal fluctuations

on the reservoirs produce backflows even under pressurized conditions, especially for short

nanotubes [40]. In order to measure the efficiency of the mCPNs at transporting water in a unidirectional fashion, we define the variable $\eta = flux / flow$, where $\eta = 1$ implies unidirectional transport and $\eta = 0$ indicates same number of permeation events on both (+x) and (−x) directions of the nanotube. It has been reported for (8,8) carbon nanotubes (CNTs) of similar dimensions as our mCPNs (~2 nm length, with 1.08 nm diameter), efficiency values of $\eta \approx 0.1$, $\eta \approx 0.4$, and $\eta \approx 0.7$, for hydrostatic applied pressures of $P \approx 36.2\ MPa$, $P \approx 181\ MPa$, and $P \approx 362\ MPa$ respectively [33]. Our results show that mCPNs are, in general, more efficient than CNTs (Fig. 6d). Even for the lowest pressure applied ($P \approx 67\ MPa$), mCPNs display efficiencies in the order of 0.7 to 0.9. Particularly, the hydrophobic mCPNs, both mCPN-Gly and mCPN-Ala, exhibit complete unidirectional transport ($\eta = 1$) for pressures as low as ~ 140 MPa, while the efficiency of (8,8) CNTs at a higher pressure of 181 MPa is around $\eta \approx 0.4$ [33]. The higher efficiency of the mCPNs can be attributed to the rougher energy landscape, compared to the smooth landscape characteristic of CNTs. The periodic energy barriers observed in our systems will decrease the reach of the effects due to the thermal fluctuations in the reservoirs.
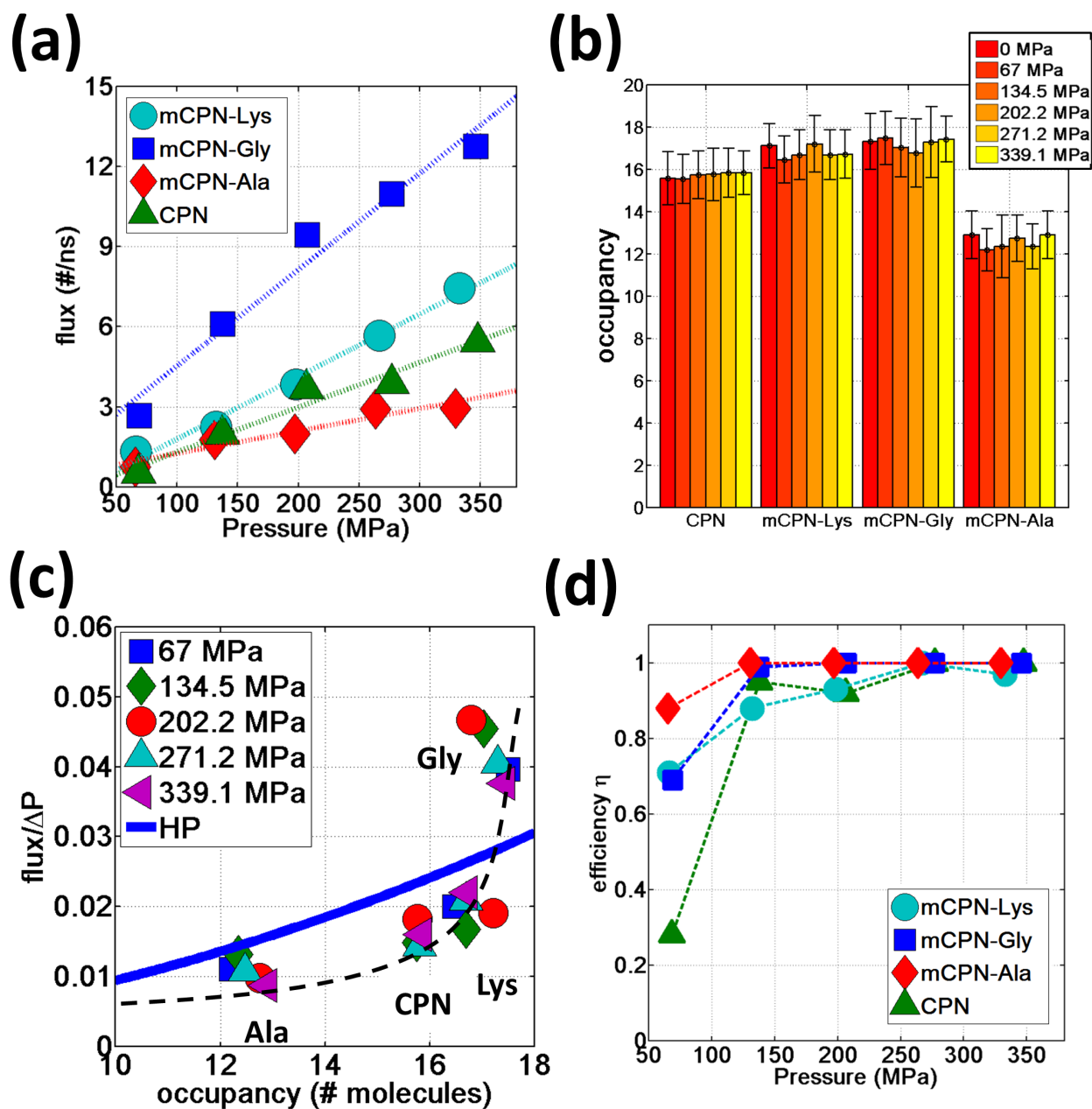
Figure 6. Water permeation under hydrostatic pressure. (a) Water flux as a function of applied pressure. (b) Average occupancy values for the different nanotubes. (c) Flux normalized by applied pressure as a function of the nanotube occupancy. A dashed black line has been added as a visual guideline. (d) Efficiency of the different nanotubes at transporting water in the direction of the gradient of the applied pressure as a function of applied pressure.

In order to gain a better understanding of how the different functional groups affect the transport properties of the mCPNs, we reconstruct the potential of mean force (PMF) profiles, which represent how the free energy of a water molecule changes as a function of the position along the nanotube. We do so by inverting the probability distributions of water molecules along the nanotube calculated over the equilibrium simulations, $\Delta F(x) = -kT \log(P(x))$. The PMF profiles are qualitatively similar for all the cases, characterized by periodic energy barriers whose magnitude depends on the steric constraints and electrostatics imposed by the functional groups on the water molecules. For the CPN, the free energy profile is characterized by periodic energy barriers of the order of the thermal energy ($kT = 0.593 \; kcal/mol$), with the free energy minima located in the inter-ring regions and other smaller local minima located in the C_α-plane regions, in agreement with previous studies [30, 32]. The minima located in the inter-ring spacing arise from the fact that the steric constraints are minimized between rings and that the water molecules favorably interact with the polar moieties of the CPs, partially compensating for the lack of coordination with respect to the bulk. The local minima at the C_α-plane regions corresponds to a weak metastable state where the water molecule is hydrated by the neighboring water molecules in the contiguous inter-ring spacing. Due to the steric repulsions imposed by the functional groups on C_α-plane regions, these metastable states are mostly absent in mCPNs. Small energy wells can be found at the interface between the nanotube and the water reservoirs, indicating that water spends significant time in the vestibules. The minimum in the vestibule is followed by an energy barrier located at both terminal rings of the nanotube. The wavy shape of the PMF profiles results in a "hopping" mechanism of water translocation. Under equilibrium conditions, and given the symmetry of the system, the PMF profiles should, in principle, be symmetric. This is the case of the CPN (Fig 7a), where the structure is relatively rigid due the constraints in the alpha carbons of the backbone. The partial lack of symmetry observed in the some of the PMF profiles of mCPNs can be attributed to two factors. The first factor is the limited

sampling of the phase space during the finite simulation time that can cause some irregularities in the profiles. The second factor is related to the fact that the unnatural amino acid is not constrained and it can fluctuate. The flexibility of the unnatural amino acid in different rings, illustrated by the snapshots shown in Figure 7, can give rise to stochastic fluctuations that may lead to deviations from a symmetric profile. In order to compare the different landscapes, we define the roughness of a PMF profile as the average energy difference between of the maxima and minima with respect to the moving average of the profile at that location: $R = n_{min}^{-1} \sum_{i=1}^{n_{min}} \left| F_i^{min} - F_{avg}(x_i) \right| + n_{max}^{-1} \sum_{i=1}^{n_{max}} \left| F_i^{max} - F_{avg}(x_i) \right|$,

where F_i^{min} and F_i^{max} are the values of the free energy of the i-th minimum or maximum respectively, n_{min} and n_{max} are the total number of minima and maxima, and $F_{avg}(x_i)$ is the value of the moving average of the profile at the location of the i-th minimum or maximum. In Figure 7(e), we show that as the roughness of profile decreases (the inverse of the roughness, which is plotted in the panel, increases) the normalized flux increases. In other words, smoother landscapes lead to higher flux. The mCPN-Gly, which achieves the highest water flux, also exhibits the smoothest free energy landscape. On the other hand the roughest landscape corresponds to the mCPN-Ala, which showed the lowest permeability.
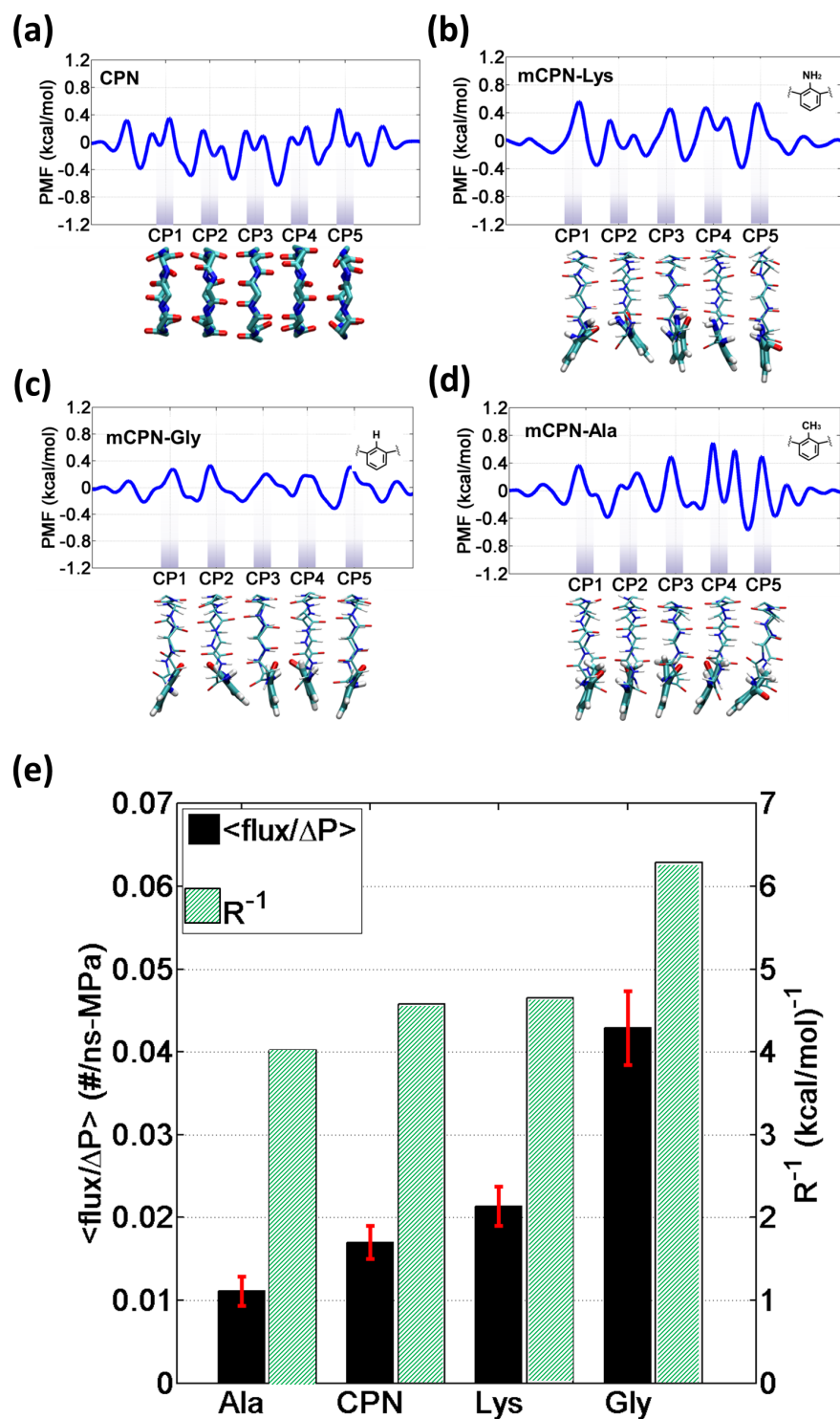
Figure 7. One-dimensional potential of mean force (PMF) profiles of water along the axis of the different nanotubes: (a) CPN, (b) mCPN-Lys, (c) mCPN-Gly, and (d) mCPN-Ala. The profiles shown are calculated using Boltzmann inversion on the water density distributions from equilibrium

simulations. Below each plot, a snapshot of the representative nanotube type is shown. (e) Flux normalized by applied pressure and inverse of the free energy roughness for the different chemistries.

It was recently reported that non-single-file water flows can be advantageous for practical applications as the decay of the permeability with the length of the nanotube (i.e. the longer the nanotube the lower the permeability) is slower than for single-file water flows [33]. This is due to the fact that concerted motion at the length-scale of the nanotube is not required for translocation of water molecules in non-single file flows. Although for biological applications, the length of the nanotubes studied here is directly relevant (the length of biological occurring channels is $\sim$ 2 nm), the scaling of flux with length of the mCPNs may have important consequences for technological applications as efficient nanopores in thin-film membranes where the nanotubes would need to span the entire film which can be tens of nanometers thick [7]. In mCPNs, we do not observe single-file water patterns and the periodic energy barriers to water permeation shown in the PMF profiles are in the order of the thermal energy. Based on these principles, we would expect slow decay of the flux when the length of mCPNs is increased, although further work is necessary to corroborate this hypothesis. Further, modulating the size of the rings by decreasing the number of amino acids is likely to lead to systems where single file flow can be achieved. The simulation methodology and transport metrics, such as the roughness criterion established here can be adopted for future studies on such systems.

Conclusions

In this paper, we showed that the insertion in the sequence of cyclic octapeptides of an unnatural amino acid with a functional group pointing inwards (mCPs) has tremendous implications in the transport properties of the nanotubes, beyond the predictions of continuum hydrodynamics. We

discovered that the particular nanoconfinement environment provided in mCPNs, determined by the supramolecular character of the nanotubes and the steric constraints and electrostatics imposed by the functional group, lead to a novel non-single-file water pattern. Along the axis of the nanotube, this structure consists on water molecules preferentially occupying the inter-ring spacing. In the cross section, water occupies the space on both sides of the functional group and the upper region of the nanotube, opposed to the location of the unnatural amino acid.

The orientation angle of water molecules in mCPNs is shown to undergo a transition upon permeation, from 30° to 150° on the left and the right of the nanotube respectively. This dipole inversion is explained by the electrostatic potential of the system, higher in the membrane and lower in the reservoirs. We showed that the specific chemistry functional group plays an important role determining the electrostatic field, and hence the orientation of water in the central region of nanotubes. In particular, the mCPN-Ala displays a distinct electrostatic signature that leads to a bimodal orientational angle distribution in the middle region of the nanotube, in contrast with the other mCPNs that exhibit flatter distributions in this transitional region.

We hypothesize here that the novel highly tunable water pattern in mCPNs (which depends on the size and polarity of the functional group of the unnatural amino acid) may have important implications on the selectivity properties of the nanotubes. The enhanced steric constraints observed in the mCPN-Lys or mCPN-Ala, compared to regular CPNs or CNTs, could potentially increase the desolvation energy barrier of ions or charged solutes, therefore increasing the rejection rate of charged species by the nanotubes. Moreover, the dipole inversion upon translocation and the absence of single-file water in the nanotubes may be useful in preventing proton translocation.

The reconstructed PMF profiles revealed periodic energy barriers whose magnitude depends on the electrostatic signature and steric constraints imposed by the functional groups. The mCPN-Gly,

characterized by small hydrophobic H groups, presented the smoothest energy landscape and highest occupancy, and therefore it exhibited the largest flux of water under pressurized conditions. In the mCPN-Lys case, the NH_2 groups impose large steric constraints that are partially compensated by the hydrophilicity of the group, leading to high occupancy values and permeability exceeding that of CPNs. The worst performer was the mCPN-Ala, which contains large hydrophobic CH_3 groups and exhibits the roughest energy landscape.

We also demonstrated that mCPNs are particularly efficient unidirectional transporters, even under unfavorable conditions of low applied pressure (~63 MPa) and short nanotube length (~ 2 nm). This is of tremendous importance for biological applications, where the length of the nanotube can be limited by the thickness of the membrane layer (~4-5 nm for lipid bilayers) and the external pressure is determined by the osmotic difference under physiological conditions.

In summary, our analysis establishes the molecular basis of water transport through a rich variety of chemistries of mCPNs, setting the cornerstone for future investigations towards the design and development of mCP-based biomimetic nanopores with heterogeneous interior chemistry.

Methods

The atomistic model consists on a nanotube embedded in a low dielectric membrane placed between two water reservoirs (Fig. 1). The simulation cell is rectangular of approximate dimensions 60 x 40 x 40 $Å^3$. Periodic boundary conditions (PBCs) are applied in all directions. Although the visualization of the system suggests the existence of two water reservoirs, due to PBCs, only one reservoir exists. The low dielectric membrane is made of toluene molecules packed in a random fashion at its equilibrium density in liquid state (0.87 g/mL). The nanotube, oriented along the x-axis, consists of 5 cyclic peptides with an approximate length of 20 Å, spanning the thickness of the membrane. The

cyclic peptides are pre-arranged in an anti-parallel beta-sheet configuration and are set apart from each other at approximately their equilibrium distance ~ 4.8 Å. The chemical makeup of the regular cyclic peptide is cyclo[(D-Ala-Leu)$_4$] and that of the chemically functionalized cyclic peptides is cyclo[(D-Ala-Leu)$_3$-D-Ala-R], where R stands for the unnatural amino-acid. The unnatural amino acid consists on a benzene ring with a functional group pointing towards the interior of the cyclic peptide. We study 3 different functional group chemistries NH$_2$, H, and CH$_3$ inspired in the Lysine, Glycine, and Alanine amino acids side chains respectively. The partial charges of the functional groups studied here are shown in Figure 1 of the Supporting Information (Fig. S1). In the following, we will refer to the different types of chemically functionalized nanotubes as mCPN followed by the abbreviation of the amino acid that the functional group mimics (e.g. mCPN-Ala). CPN stands for a nanotube formed by regular octapeptides without unnatural amino acid. All the nanotube types are simulated under equilibrium conditions and 5 levels of hydrostatic pressure differences (from ~67 MPa to ~339 MPa), making a total of 24 different cases. All the nanotubes are homomeric (i.e. all the cyclic peptides in the nanotube have the same chemistry).

All the simulations presented in this paper are carried out using the parallel molecular dynamics software NAMD2 [41]. The molecular visualization package VMD [42], in combination with TCL scripts and the program Matlab, have been used for the post process analysis. The CHARMM36 force-field [43] is used for the protein nanotubes. We use a TIP3 standard model for water [44]. The CHARMM general force-field (CGenFF) is used for the toluene membrane. CHARMM36 and CGenFF are fully compatible force-fields. The unnatural amino acids studied here (Fig. 2) are not fully parameterized in the CHARMM force-field. In order to find the missing parameters, we use the software ParamChem 0.9.7.1 [45] with the CGenFF 2b8 force-field [46]. The software outputs the values for the missing parameters together with a penalty measurement that estimates the quality of the prediction. Penalty values larger than 50 are considered poor quality and require extensive validation. All the

penalties obtained for the parameters in this study are within the acceptable range, with most of the

parameters having penalties of zero and only a few parameters with penalties in the range from 10 to

20. The parameters corresponding to the angles and dihedrals of the peptide bond between the

unnatural and the regular amino-acids are set equal to the peptide bond between two regular amino-

acids.

The same simulation protocol is followed for all the cases. A timestep of 1 fs is used for all the

simulations. After minimization of the system for 1000 steps using the conjugate gradient and line

search algorithm, we equilibrate the system in the NPT ensemble (constant number of particles,

pressure and temperature) at T = 298 K, P = 1 atm. The pressure is controlled using a modified

Nosé-Hoover method in which Langevin dynamics is used to control the fluctuations in the barostat

[47]. A damping coefficient of 7 ps^{-1} is used to control the temperature. The electrostatic interactions

are calculated using the particle mesh Ewald (PME) method [48]. We equilibrate the system for 1.5 ns,

during which the C_α of the CPs are constrained in the x-direction (the longitudinal direction of the

nanotube). Under these constraints the CPs are allowed to rotate and move just in the plane of the

rings, maintaining the inter-ring equilibrium distance. In the absence of constraints, the CPN has

been seen to tilt in low dielectric membranes [49-51]. While this process may be of interest in some

context, here we are only interested on the transport mechanisms across the nanotube. Our

constraints, despite preventing the tilt of the nanotube, still permit ring rotation and in-plane

displacement that allow maximization the inter-ring hydrogen bond formation and therefore

minimize the energy of the system. Similar protocols have been used in previous studies on the

transport in regular CPNs [30, 32, 52].

After equilibration, we study water transport through the nanotubes under both, equilibrium

conditions (Eq-MD) and under different levels of hydrostatic pressure. All the simulations, after

equilibration of the system, are carried out using the NVT ensemble (constant number of particles, volume and temperature) at T = 298 K. To avoid large displacements of the nanotube or the membrane in the x-direction due to the applied pressure, the C_α of the cyclic peptides and the carbon linking the methyl group and the benzene ring in the toluene molecules are constrained by harmonic springs with a spring constant of 10 kcal/mol- Å^2 to their original positions. The same constraints are applied during the Eq-MD simulations. The Eq-MD simulations are run for 50 ns, while the simulations under pressurized flow, more computationally expensive, are run for approximately 20 ns after the equilibration process. The hydrostatic pressure difference is established across the membrane following the method proposed by Zhu et al [39]. In this method a constant force, f, is applied to the oxygen atoms of the water molecules in a system with PBCs. In order to minimize the artifacts introduced by the external force in the transport mechanisms of water close to the nanotubes, we only apply the force to the water molecules in the reservoir that are further than 3 Å from the nanotube backbone. The pressure difference induced, assuming a stationary state, is $\Delta P = nf / A$, where n is the number of water molecules and A is the cross-section of the system. We study 5 different pressure differences: 67, 134.5, 202.2, 271.2, and 339.1 MPa.

In order to calculate the electrostatic potential heat maps and one-dimensional profiles along the nanotube axis we used the PMEPot plugin from the VMD program [53]. This software allows calculating a smoothed electrostatic potential grid of the system using the Particle Mesh Ewald (PME) method. The mean electrostatic field of the system is calculated as the average the instantaneous electric field from 5,000 frames taken evenly spaced through the entire simulation. For this calculation, we use a grid of 60 x 44 x 44 points in the x, y and z directions respectively and a Ewald factor of 0.25.

The results reported here should be treated as semi-quantitative due to their possible dependence on the choice of atomistic force-field, model of water employed or value of the thermostat damping parameter [54]. However, the observed trends are expected to be hold in a physical context.

Acknowledgements

Supporting Information

Supporting information is available from the author. It contains three figures regarding some details of the analysis presented here. The first figure shows the charge distribution of the different functional groups explored. The second and third figures contain density profiles of water along orthogonal directions of the nanotubes cross section.

References

1. M. A. Shannon, P. W. Bohn, M. Elimelech, J. G. Georgiadis, B. J. Marinas and A. M. Mayes, *Nature*, 2008, 452, 301-310.
2. T. C. Merkel, H. Lin, X. Wei and R. Baker, *J. Membr. Sci.*, 2010, 359, 126-139.
3. B. C. H. Steele and A. Heinzel, *Nature*, 2001, 414, 345-352.
4. Z. Niu, L. Liu, L. Zhang and X. Chen, *Small*, 2014, 10, 3434-3441.
5. B. J. Hinds, N. Chopra, T. Rantell, R. Andrews, V. Gavalas and L. G. Bachas, *Science*, 2004, 303, 62-65.
6. J. K. Holt, H. G. Park, Y. Wang, M. Stadermann, A. B. Artyukhin, C. P. Grigoropoulos, A. Noy and O. Bakajin, *Science*, 2006, 312, 1034-1037.
7. T. Xu, N. Zhao, F. Ren, R. Hourani, M. T. Lee, J. Y. Shu, S. Mao and B. A. Helms, *ACS Nano*, 2011, 5, 1376-1384.

8. H. Verweij, M. C. Schillo and J. Li, *Small*, 2007, 3, 1996-2004.
9. E. Gouaux and R. MacKinnon, *Science*, 2005, 310, 1461-1465.
10. B. L. de Groot and H. Grubmüller, *Science*, 2001, 294, 2353-2357.
11. S. Bernèche and B. Roux, *Structure*, 2005, 13, 591-600.
12. L. Ruiz, P. Vonachen, T. D. Lazzara, T. Xu and S. Keten, *Nanotechnology*, 2013, 24.
13. A. C. D. Jennifer and Ç. Tahir, *Nanotechnology*, 2010, 21, 115703.
14. R. Hourani, C. Zhang, R. van der Weegen, L. Ruiz, C. Li, S. Keten, B. A. Helms and T. Xu, *J. Am. Chem. Soc.*, 2011, 133, 15296-15299.
15. R. Chapman, M. Danial, M. L. Koh, K. A. Jolliffe and S. Perrier, *Chem. Soc. Rev.*, 2012, 41, 6023-6041.
16. A. Kalra, S. Garde and G. Hummer, *Proceedings of the National Academy of Sciences*, 2003, 100, 10175-10180.
17. L. S. King, D. Kozono and P. Agre, *Nat. Rev. Mol. Cell Biol.*, 2004, 5, 687-698.
18. M. Kumar, M. Grzelakowski, J. Zilles, M. Clark and W. Meier, *Proceedings of the National Academy of Sciences*, 2007, 104, 20719-20724.
19. T. Humplik, J. Lee, S. C. O'Hern, B. A. Fellman, M. A. Baig, S. F. Hassan, M. A. Atieh, F. Rahman, T. Laoui, R. Karnik and E. N. Wang, *Nanotechnology*, 2011, 22, 292001.
20. B. Corry, *The Journal of Physical Chemistry B*, 2007, 112, 1427-1434.
21. N. Savage and M. Diallo, *J Nanopart Res*, 2005, 7, 331-342.
22. D. Cohen-Tanugi and J. C. Grossman, *Nano Lett.*, 2012, 12, 3602-3608.
23. Q. Chen, L. Meng, Q. Li, D. Wang, W. Guo, Z. Shuai and L. Jiang, *Small*, 2011, 7, 2225-2231.
24. N. Modi, M. Winterhalter and U. Kleinekathofer, *Nanoscale*, 2012, 4, 6166-6180.
25. G. Hummer, J. C. Rasaiah and J. P. Noworyta, *Nature*, 2001, 414, 188-190.
26. O. Beckstein and M. S. P. Sansom, *Proceedings of the National Academy of Sciences*, 2003, 100, 7063-7068.
27. S. Joseph and N. R. Aluru, *Nano Lett.*, 2008, 8, 452-458.
28. M. Thomas, B. Corry and T. A. Hilder, *Small*, 2014, 10, 1453-1465.
29. M. Engels, D. Bashford and M. R. Ghadiri, *J. Am. Chem. Soc.*, 1995, 117, 9151-9158.
30. J. Liu, J. Fan, M. Tang and W. Zhou, *The Journal of Physical Chemistry A*, 2010, 114, 2376-2383.
31. J. Liu, J. Fan, M. Tang, M. Cen, J. Yan, Z. Liu and W. Zhou, *The Journal of Physical Chemistry B*, 2010, 114, 12183-12192.
32. J. Comer, F. Dehez, W. Cai and C. Chipot, *The Journal of Physical Chemistry C*, 2013, 117, 26797-26803.
33. J. Su and H. Guo, *The Journal of Physical Chemistry B*, 2012, 116, 5925-5932.
34. C. Peter and G. Hummer, *Biophys. J.*, 89, 2222-2234.
35. M. Ø. Jensen, E. Tajkhorshid and K. Schulten, *Biophys. J.*, 85, 2884-2899.
36. I. Hanasaki and A. Nakatani, *The Journal of Chemical Physics*, 2006, 124, -.
37. J. A. Thomas and A. J. H. McGaughey, *Nano Lett.*, 2008, 8, 2788-2793.
38. M. Borgnia, S. Nielsen, A. Engel and P. Agre, *Annu. Rev. Biochem.*, 1999, 68, 425-458.
39. F. Zhu, E. Tajkhorshid and K. Schulten, *Biophys. J.*, 2002, 83, 154-160.
40. G. Zuo, R. Shen, S. Ma and W. Guo, *ACS Nano*, 2009, 4, 205-210.
41. J. C. Phillips, R. Braun, W. Wang, J. Gumbart, E. Tajkhorshid, E. Villa, C. Chipot, R. D. Skeel, L. Kalé and K. Schulten, *J. Comput. Chem.*, 2005, 26, 1781-1802.
42. W. Humphrey, A. Dalke and K. Schulten, *Journal of Molecular Graphics*, 1996, 14, 33-38.
43. R. B. Best, X. Zhu, J. Shim, P. E. M. Lopes, J. Mittal, M. Feig and A. D. MacKerell, *J. Chem. Theory Comput.*, 2012, 8, 3257-3273.
44. W. L. Jorgensen, J. Chandrasekhar, J. D. Madura, R. W. Impey and M. L. Klein, *The Journal of Chemical Physics*, 1983, 79, 926-935.
45. K. Vanommeslaeghe and A. D. MacKerell, *J. Chem. Inf. Model.*, 2012, 52, 3144-3154.
46. K. Vanommeslaeghe, E. Hatcher, C. Acharya, S. Kundu, S. Zhong, J. Shim, E. Darian, O. Guvench, P. Lopes, I. Vorobyov and A. D. Mackerell, *J. Comput. Chem.*, 2010, 31, 671-690.

47.   G. J. Martyna, D. J. Tobias and M. L. Klein, *The Journal of Chemical Physics*, 1994, 101, 4177-4189.
48.   U. Essmann, L. Perera, M. L. Berkowitz, T. Darden, H. Lee and L. G. Pedersen, *The Journal of Chemical Physics*, 1995, 103, 8577-8593.
49.   H. S. Kim, J. D. Hartgerink and M. R. Ghadiri, *J. Am. Chem. Soc.*, 1998, 120, 4417-4424.
50.   H. Hwang, G. C. Schatz and M. A. Ratner, *The Journal of Physical Chemistry A*, 2008, 113, 4780-4787.
51.   M. Tarek, B. Maigret and C. Chipot, *Biophys. J.*, 85, 2287-2298.
52.   H. Hwang, G. C. Schatz and M. A. Ratner, *The Journal of Physical Chemistry B*, 2006, 110, 26448-26460.
53.   A. Aksimentiev and K. Schulten, *Biophys. J.*, 2005, 88, 3745-3761.
54.   P. Mark and L. Nilsson, *The Journal of Physical Chemistry A*, 2001, 105, 9954-9960.